Implementation of a non-axisymmetric magnetic configuration in SOLEDGE3X to simulate 3D toroidal magnetic ripple effects: Application to WEST

Raffael Düll, Guido Ciraolo, Hugo Bufferand, Eric Serre, Virginia Quadri, Nicolas Rivals, Patrick Tamain, Srikanth Sureshkumar, Naren Varadarajan

Nuclear Materials and Energy 41 (2024) 101807

Contents lists available at ScienceDirect

Nuclear Materials and Energy

journal homepage: www.elsevier.com/locate/nme

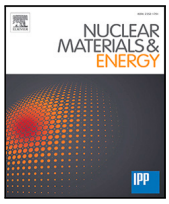

Implementation of a non-axisymmetric magnetic configuration in SOLEDGE3X to simulate 3D toroidal magnetic ripple effects: Application to WEST

Raffael Düll [a,*], Guido Ciraolo [a], Hugo Bufferand [a], Eric Serre [b], Virginia Quadri [a], Nicolas Rivals [a], Patrick Tamain [a], Srikanth Sureshkumar [a], Naren Varadarajan [a]

[a] IRFM/CEA, Cadarache, 13108, St-Paul-Lez-Durance, France
[b] Aix Marseille Université, CNRS, Centrale Marseille, M2P2, 13451, Marseille, France

ARTICLE INFO

Keywords:
Edge plasma
SOLEDGE3X
Magnetic ripple
Simulation
WEST tokamak
Non-axisymmetric

ABSTRACT

The fluid-drift code SOLEDGE3X, developed by CEA/IRFM in collaboration with Aix-Marseille University, is a powerful tool for simulating transport and turbulence in tokamak edge plasmas with axisymmetric magnetic configurations. In tokamaks such as WEST, the pronounced toroidal magnetic ripple significantly affects plasma confinement and power exhaust, modulating both the poloidal and toroidal components of the equilibrium field. Using a discrete Biot–Savart law, the ripple field is calculated as a magnetic perturbation on the SOLEDGE3X mesh. The transport model and parallel gradient solvers have been enhanced to incorporate the new radial magnetic field component. Preliminary simulations of a WEST scenario reveal a heat deposition pattern in the divertor region consistent with observations from infrared camera experiments.

1. Introduction

Power exhaust is a major concern in magnetic fusion research. Accurately predicting the heat load on the divertor plates is essential for the design and operation of current and future tokamaks. Estimates for the International Thermonuclear Experimental Reactor (ITER), the most powerful device currently under construction, indicate maximum local heat loads close to material limits [1]. For this reason, it is important to study the transport of heat and particle fluxes in present experiments, coupling the experimental analysis with modeling efforts using dedicated numerical tools.

Experiments conducted on the tungsten environment steady-state tokamak (WEST) at CEA in Cadarache, France [2], have demonstrated that the heat deposition on the divertor targets is not uniform in the toroidal direction. A “snake skin” pattern (see Fig. 1), with alternating local maxima, appears on the inner and outer divertor targets. Reconstructions from infrared camera images exhibit a considerable difference between peaks and lows along a target line. These variations correlate with the disposition of the toroidal magnetic field coils, which locally modify the field lines and amplitude. This effect is known as magnetic ripple [3] and causes hotspots on the divertor targets in any tokamak design [4]. It is particularly pronounced on WEST, where the 18 coils cause strong variations in the amplitude of the magnetic field **B** up to 7%. For example, fast ions trapped in the toroidal magnetic field ripple have been found to be responsible for significant power losses [5,6]. Moreover, it is important to determine the impact of this toroidal modulation on impurity transport, in particular on tungsten contamination of the core [7]. The strong ripple has played an important role in the design of edge components [8] and heating systems [9], motivating the development of ripple reduction strategies, such as magnetic inserts [10] or saddle coils [11], which have been incorporated in later machines.

SOLEDGE3X is a powerful fluid code for scrape-off-layer (SOL) and edge plasma analysis. The simulation domain extends from the far core across the separatrix up to the first wall in complex geometries. Its full model is capable of simulating turbulence driven by resistive drift-wave and interchange instabilities [12] with advanced fluid closures [13] and interactions with recycling neutrals [14]. A “transport” mode, where cross-field transport is approximated with effective diffusion coefficients, allows simulations to run until convergence on large machines like ITER [15] or JT-60SA [16]. Applications of this code include studies on impurity transport [17], heat exhaust [18], and detachment regimes in the divertor [19].

In its current form, SOLEDGE3X can address 2D and 3D axisymmetric configurations as well as 3D non-axisymmetric wall geometries [20], but still requires a 3D axisymmetric magnetic field. Therefore, toroidal

* Corresponding author.
E-mail address: raffael.duell@gmx.de (R. Düll).

https://doi.org/10.1016/j.nme.2024.101807
Received 5 July 2024; Received in revised form 30 October 2024; Accepted 5 November 2024
Available online 14 November 2024

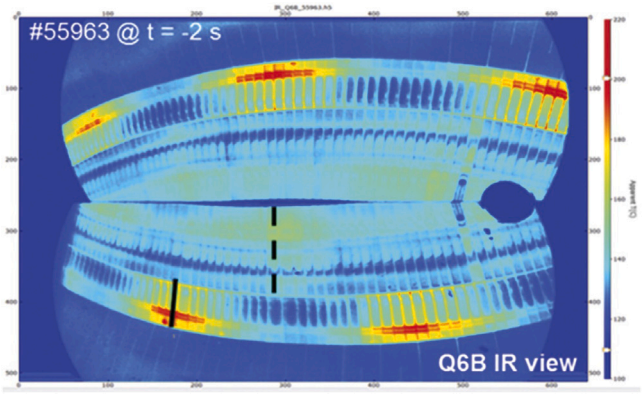

Fig. 1. Infrared camera view of the divertor target, taken from [2]. Red zones correspond to hot regions with high heat deposition. One can see the "snake skin" pattern, where the maximal intensity alternates between the inner and outer strike points.

variations of the magnetic field due to ripple could not be taken into account. Moreover, matching simulation results to experimental data is made difficult by the toroidal locality of Langmuir probes and their consequent susceptibility to ripple effects. Recent developments in the turbulence model have introduced electromagnetic effects [21], where magnetic field lines are perturbed by fluctuations of the magnetic vector potential. In this paper, we demonstrate that the new implementations can be used not only for plasma-induced perturbations but also for external perturbations of the axisymmetric magnetic field. This paves the way for ripple simulations in SOLEDGE3X and will be applied to a WEST scenario in this paper.

2. Generation of a non-axisymmetric magnetic configuration

The SOLEDGE3X framework is capable of addressing magnetic configurations with singularities at one or more X-points. Constructed by a combination of a toroidal field, $\mathbf{B}_t$, and a poloidal field, $\mathbf{B}_{pol}$, the expression for the magnetic field is:

$$\mathbf{B}_{axi} = \mathbf{B}_t + \mathbf{B}_{pol} = F\nabla\varphi + \nabla\Psi \times \nabla\varphi \tag{1}$$

where φ represents the toroidal angle. The toroidal field $\mathbf{B}_t$ is derived from a toroidal flux F and $\mathbf{B}_{pol}$ from a poloidal flux function Ψ.

For high numerical accuracy, the meshing in SOLEDGE3X is aligned to magnetic flux surfaces, treating singularities with a multi-domain decomposition shown in Fig. 2. On top of this axisymmetric basis, we calculate the ripple perturbation of the magnetic field induced by the toroidal distribution of the toroidal field coils. For that, we simplify each coil to a single, circular wire. We first discretize each of the N_c coils into N_{seg} segments. For every cell in the SOLEDGE3X grid, we then calculate the magnetic field associated with the coils using the Biot–Savart law:

$$\mathbf{B}_{ripple} = \frac{\mu_0}{4\pi} I_c \sum_{i=1}^{N_c} \sum_{j=1}^{N_{seg}} \frac{\mathbf{d}_{i,j} \times \left(\mathbf{s}_{i,j+1} - \mathbf{s}_{i,j}\right)}{\left\|\mathbf{d}_{i,j}\right\|^3} \tag{2}$$

where the coil current I_c corresponds to the nominal coil current times the number of wire turns in a coil, $\mathbf{s}_{i,j}$ represents the start and end locations of each coil segment, and $\mathbf{d}_{i,j}$ is the vector from each mesh point to the segment center. To avoid accounting for the axisymmetric component of the magnetic field twice, we define the perturbation field as the toroidal fluctuations of the ripple field:

$$\mathbf{B}_{pert} = \mathbf{B}_{ripple} - \left\langle \mathbf{B}_{ripple} \right\rangle_{\varphi} \tag{3}$$

Together with the axisymmetric part from Eq. (1), the equilibrium magnetic field as applied to the simulation is given by:

$$\mathbf{B} = \mathbf{B}_{axi} + \mathbf{B}_{pert} \tag{4}$$

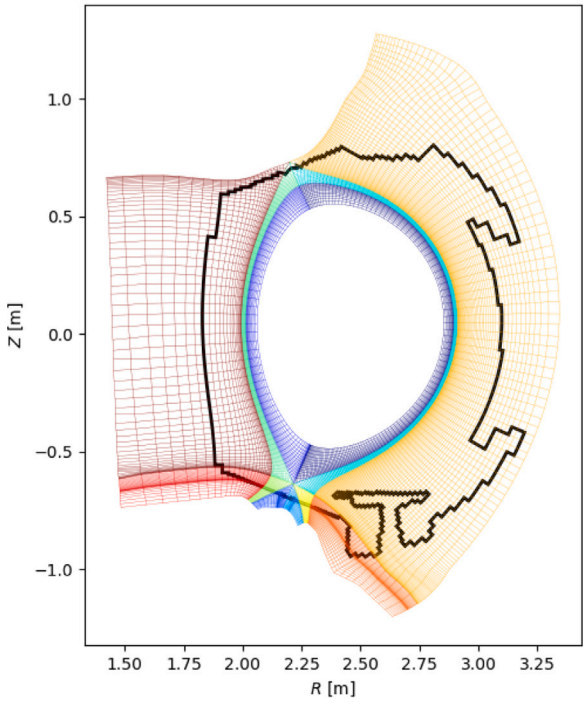

Fig. 2. Exemplary SOLEDGE3X mesh for a WEST single-null geometry.

Table 1
Technical parameters of the toroidal field coils used to generate the ripple field for the WEST tokamak.

Number of coils	N_c	18
Major coil radius	R_c	2.443 m
Minor coil radius	a_c	1.292 m
Nominal coil current	I_c	1.2 kA
Number of wire turns	N_{turns}	2028

This strategy is now applied to compute the magnetic field ripple for the WEST tokamak, with the coil parameters described in Table 1. The ripple has a twofold impact on the magnetic equilibrium. A toroidal perturbation field, as shown in Fig. 3(a), modifies $\mathbf{B}_t$ with local maxima located at the coils' positions and minima midway between two coils. The perturbation vanishes at $\pi/2$ and $3\pi/2$ of a ripple period. Conversely, the radial perturbation in Fig. 3(b) vanishes at the coils and midway, and modifies the poloidal field $\mathbf{B}_{pol}$.

Even if the amplitude of the ripple field is small compared to the axisymmetric one, it strongly impacts the poloidal field $\mathbf{B}_{pol}$ from one poloidal plane to another. As $\mathbf{B}_{pol}$ approaches zero at X-points, the radial perturbation $\mathbf{B}^{\Psi}_{pert}$ induced by the coils dominates over the axisymmetric component. In Fig. 4, we observe that the X-point based on B_{pol} shifts by about 4.1 cm towards the high-field side at the maximal radial perturbation and by 2.7 cm inwards at the minimum.

However, this does not mean that the last closed flux surface (LCFS) experiences such a strong modulation. Indeed, the toroidal field $\mathbf{B}_t$ imposes a consistent structure across poloidal planes. Tracing magnetic field lines, we observe in Fig. 5 that seed points launched from the same position on different poloidal planes are only modulated by a few millimeters. Magnetic islands at rational surfaces have a similarly small width, which correspond to the large mode numbers (e.g., $n = 18$ for the TF coil configuration in WEST). Key features of the configuration, such as the separatrix, remain almost unaffected; however, the strong toroidal modulation of the singularity in $\mathbf{B}_p$ means that the magnetic field in the vicinity of the X-point becomes stochastic.

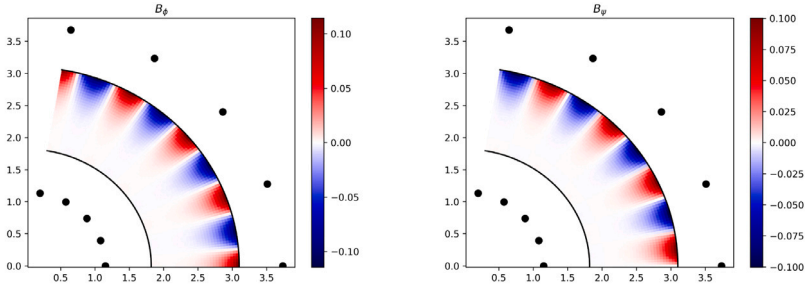

(a) Toroidal component B^{φ}_{pert}, in T (b) Radial component B^{ψ}_{pert}, in T

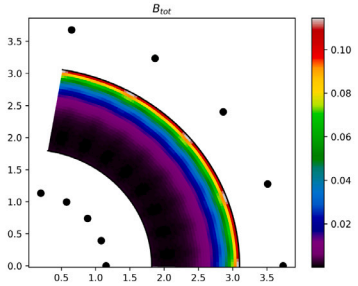

(c) Amplitude of the field $\left\|\mathbf{B}_{pert}\right\|$, in T

Fig. 3. Top views of the perturbated field $\mathbf{B}_{pert}$ on the WEST tokamak at the mid-plane. The black dots indicate the position of the toroidal field coils. The amplitude of the perturbated field remains much smaller than the axisymmetric component, whose amplitude ranges around 1T.

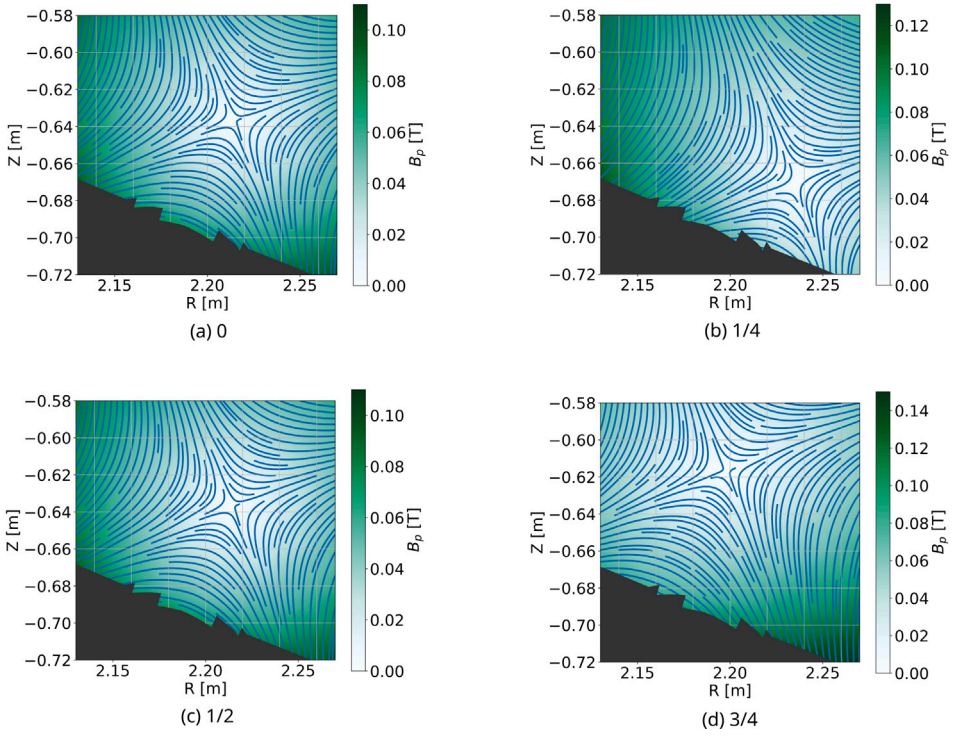

Fig. 4. Map of the poloidal field B_{pol} [T] at several poloidal planes within a ripple period around the lower X-point and the divertor targets. Streamlines are supperposed to the fields to better visualize the position of the X-point and the separatrix at the divertor. The phase shifts 0 and 1/2 with respect to the coil positions are identical to the axisymmetric configuration as B^{ψ}_{pert} vanishes while the planes at 1/4 and 3/4 correspond to the respective maximum and minimum of B^{ψ}_{pert}.

3. Transport model in SOLEDGE3X

Boltzmann's statistical description of gases extends to plasmas, allowing Braginskii [22] to derive essential transport equations for the subsequent model. In the SOL region, plasma has a high density and low temperature, with a mean free path λ_C of about 1 meter and a connection length of around 100 meters [23]. This high collisionality makes the fluid approach to plasma modeling particularly effective.

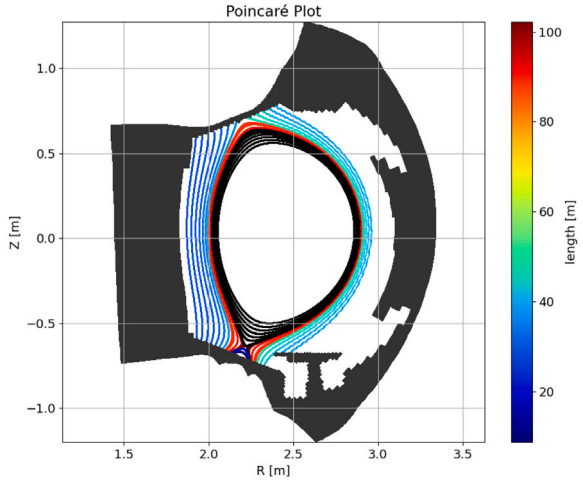

(a) Full poloidal plane

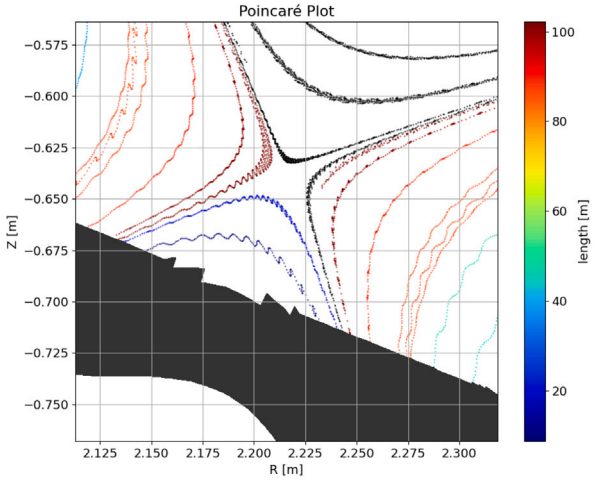

(b) Zoom on the X-point region

Fig. 5. Poincaré plot at coil-aligned poloidal planes. Seed points are uniformly distributed on the mid-plane along the radial and toroidal directions. Because of the periodicity of the perturbated field, each point corresponds to a field line crossing any of the N_c planes aligned with a coil. The total length of a field line from wall to wall translates in its color, black standing for an infinite closed field line. (For interpretation of the references to color in this figure legend, the reader is referred to the web version of this article.)

We solve the conservation Eqs. (5)–(7) for the ion density n_i, ion parallel momentum $nv_{\parallel,i}$ and electron/ion temperature T_α.

$$\partial_t n_i + \boldsymbol{\nabla}\cdot\left[n_i\left(v_\parallel \mathbf{b} + \mathbf{v}_\perp\right)\right] = S_{n_i} - \mathcal{D}_\perp(n_i) \tag{5}$$

$$m_i\partial_t n_i v_{\parallel,i} + m_i\boldsymbol{\nabla}\cdot\left[n_i v_{\parallel,i}\left(v_\parallel \mathbf{b} + \mathbf{v}_\perp\right)\right] = \boldsymbol{\nabla}\cdot\left[\nu_\parallel \boldsymbol{\nabla}_\parallel v_{\parallel,i}\mathbf{b}\right] + S_{n_i v_{\parallel,i}} + R_{n_i v_{\parallel,i}} - \mathcal{D}_\perp(n_i v_{\parallel,i}) \tag{6}$$

$$\partial_t T_\alpha + \boldsymbol{\nabla}\cdot\left[T_\alpha\left(v_\parallel \mathbf{b} + \mathbf{v}_\perp\right)\right] = \boldsymbol{\nabla}\cdot\left[\nu_\parallel v_\parallel \boldsymbol{\nabla}_\parallel v_{\parallel,i}\mathbf{b}\right] + \boldsymbol{\nabla}\cdot\left[\kappa_\parallel \boldsymbol{\nabla}_\parallel T_\alpha \mathbf{b}\right] + S_{T_\alpha} + R_{T_\alpha} - \mathcal{D}_\perp(T_\alpha) \tag{7}$$

The electron density and momentum are calculated a posteriori with the quasi-neutrality (8) and ambipolarity (9) assumptions.

$$n_e = \frac{1}{e}\sum_i q_i n_i \tag{8}$$

$$n_e v_{\parallel,e} = \frac{1}{e}\sum_i q_i n_i v_{\parallel,i} \tag{9}$$

The parallel viscosity $\nu_\parallel$ and heat resistivity $\kappa_\parallel$ are known from the Spitzer-Härm model [24]. Ionization and recombination processes lead to source terms S. Further pressure, heat flux and Zhdanov friction [25,26] terms are represented by the residual term R, for which a more detailed description can be found in [12,27]. Perpendicular diffusion $\mathcal{D}_\perp(\circ) = \boldsymbol{\nabla}\cdot(D_\perp\boldsymbol{\nabla}_\perp\circ)$ emulates cross-field transport.

The magnetic ripple perturbation impacts all terms dependent on the magnetic unit vector $\mathbf{b} = \mathbf{B}/\|\mathbf{B}\|$, substantially modifying parallel gradients $\boldsymbol{\nabla}_\parallel X = \mathbf{b}\cdot\boldsymbol{\nabla}X$, which now include a radial component in addition to the poloidal and toroidal components.

4. Numerical implementation

The magnetic ripple can be easily added to an existing magnetic configuration for SOLEDGE3X. Before executing the simulation, the procedure detailed in Section 2 is used to calculate the perturbed field on each cell of a provided SOLEDGE3X mesh. Together with the unchanged axisymmetric equilibrium field, the total magnetic field is calculated and subsequently used in the simulation.

One specificity of the SOLEDGE3X code has always been its structured grid aligned to magnetic flux-surfaces. With the perturbed field, this alignment becomes more challenging, especially with the introduction of a radial component to the magnetic field and the varying location of the X-point as seen in Fig. 4. As the perturbation remains small compared to the axisymmetric part, the meshing remains aligned to $\mathbf{B}_{axi}$, and we treat ripple advection similarly to first-order drifts.

The conservation equations evolve with an implicit-explicit time integration scheme, where all advection and perpendicular diffusion terms are advanced explicitly in time. However, the parallel diffusion on $v_\parallel$ and T_α requires iterative solvers to avoid restrictions on the timestep size due to the rapid dynamics linked to viscous and resistive effects. With only the axisymmetric field, the flux-surface-aligned grid in SOLEDGE3X allows for the neat decoupling of this implicit system into one 2D system per flux surface. With the full magnetic configuration, the radial component of the ripple perturbations inevitably introduces coupling between flux surfaces in the system. This necessitates solving a single 3D system for the entire simulation domain, involving a considerable computational overhead. To prevent numerical diffusion from this non-aligned operator, a new discretization that isolates radial (perturbed) from poloidal and toroidal (equilibrium + perturbed) diffusion was developed. Gradients in the equilibrium direction are calculated solely on the corresponding flux surface to avoid artificial radial spreading, and the scheme converges to the original discretization of the operator as perturbations approach zero [28].

5. Application to a WEST scenario

To demonstrate the newly implemented feature, we perform a SOLEDGE3X simulation on a WEST scenario with ripple. We consider a simple deuterium plasma with recycling fluid neutrals (recycling coefficient 98%). The core density fixed tp 2×10^{19} particles/m^3, and 1 MW Ohmic heating is equally applied to electrons and ions. Cross-field transport is emulated by a constant diffusion of 0.3 m^2/s for particles and 1.0 m^2/s for electron and ion heat diffusion. To cope with low densities in the far SOL, the electron and ion heat fluxes are limited to 0.2 and 2.0 of the free-streaming energy flux, and the viscous stress tensor is limited to 0.5 of the pressure.

To reduce numerical costs, we only simulate one ripple period, or 1/18th of the full torus, and periodically expand the simulated plasma in the toroidal direction. The simulation contains 250,000 cells spread over 16 poloidal planes and was run on 384 processors of the MARCONI computing center [29] for 20 ms simulated plasma time. The plasma

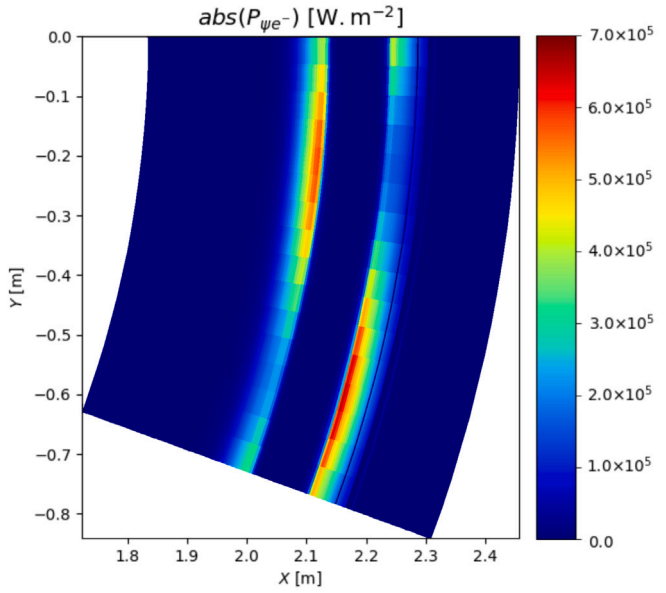

Fig. 6. Calculated electron wall heat flux in the divertor region from the SOLEDGE3X simulation. View on the target from the top for one ripple period.

has not yet reached a converged state, but is sufficiently stable to observe ripple-induced phenomena.

In Fig. 6, the heat fluxes originating at the core source reach the divertor target with maximal heat loads that alternate between the inner and the outer strike point with the toroidal coordinate. It has a strong resemblance with the "snake skin" pattern in Fig. 1 observed on infrared imagery during the tokamak operation.

6. Conclusion

The incorporation of magnetic ripple perturbations into the SOLEDGE3X framework significantly enhances its capability to simulate complex magnetic configurations in tokamaks. Using the Biot–Savart law to calculate the ripple effects, this study exhibits the impact of the toroidal magnetic ripple on the magnetic equilibrium configuration in the WEST tokamak. These perturbations both affect the poloidal and the radial component of the axisymmetric magnetic equilibrium, with an important modulation of the poloidal field.

The perturbed magnetic field has been integrated into all parallel advection and gradient terms of the SOLEDGE3X transport model. The radial component of the poloidal perturbation field required major refactoring of the transport model because the mesh remains aligned to axisymmetric flux surfaces. Parallel fluxes now occur in all three directions in the curvilinear coordinates. Consequently, implicit solvers for the heat and viscosity problems are now applied to full-domain 3D systems instead of independent 2D systems on each flux surface, resulting in additional computational costs.

Simulations on a realistic WEST geometry demonstrate the new capability to perform simulations in a non-axisymmetric magnetic configuration. Key features of magnetic ripple, such as the modulation of heat loads on the divertor strike points along the toroidal coordinate, are successfully recovered.

With this new implementation, it will be possible to explore new physics, such as ripple effects on tungsten core contamination or improved predictions of power exhaust in tokamaks. Additionally, this enhancement allows for better comparisons between simulation and experimental data due to the toroidal locality of several plasma diagnostics.

CRediT authorship contribution statement

Raffael Düll: Writing – review & editing, Writing – original draft, Visualization, Validation, Software, Methodology, Investigation, Formal analysis, Data curation, Conceptualization. **Guido Ciraolo:** Writing – review & editing, Writing – original draft, Project administration, Funding acquisition. **Hugo Bufferand:** Supervision, Software, Investigation, Funding acquisition. **Eric Serre:** Supervision. **Virginia Quadri:** Software. **Nicolas Rivals:** Visualization, Validation, Software, Methodology. **Patrick Tamain:** Software, Funding acquisition. **Srikanth Sureshkumar:** Software. **Naren Varadarajan:** Software.

Declaration of competing interest

The authors declare that they have no known competing financial interests or personal relationships that could have appeared to influence the work reported in this paper.

Acknowledgments

This work has been carried out within the framework of the EUROfusion Consortium, funded by the European Union via the Euratom Research and Training Programme (Grant Agreement No 101052200 — EUROfusion). Views and opinions expressed are however those of the author(s) only and do not necessarily reflect those of the European Union or the European Commission. Neither the European Union nor the European Commission can be held responsible for them. This work was granted access to the HPC resources of the EUROfusion High Performance Computer (Marconi-Fusion) under the project TSVV3.

Data availability

Data will be made available on request.

References

[1] J.P. Gunn, S. Carpentier-Chouchana, F. Escourbiac, T. Hirai, S. Panayotis, R. Pitts, Y. Corre, R. Dejarnac, M. Firdaouss, M. Kočan, et al., Surface heat loads on the ITER divertor vertical targets, Nucl. Fusion 57 (4) (2017) 046025.

[2] J. Bucalossi, J. Achard, O. Agullo, T. Alarcon, L. Allegretti, H. Ancher, G. Antar, S. Antusch, V. Anzallo, C. Arnas, D. Arranger, J. Artaud, M. Aumeunier, S. Baek, X. Bai, J. Balbin, C. Balorin, T. Barbui, A. Barbuti, J. Barlerin, V. Basiuk, T. Batal, O. Baulaigue, A. Bec, M. Bécoulet, E. Benoit, E. Benard, J. Benard, N. Bertelli, E. Bertrand, P. Beyer, J. Bielecki, P. Bienvenu, R. Bisson, V. Bobkov, G. Bodner, C. Bottereau, C. Bouchand, F. Bouquey, C. Bourdelle, J. Bourg, S. Brezinsek, F. Brochard, C. Brun, V. Bruno, H. Bufferand, A. Bureau, S. Burles, Y. Camenen, B. Cantone, E. Caprin, S. Carpentier, G. Caulier, N. Chanet, O. Chellai, Y. Chen, M. Chernyshova, P. Chmielewski, W. Choe, A. Chomiczewska, G. Ciraolo, F. Clairet, J. Coenen, L. Colas, G. Colledani, J. Colnel, P. Coquillat, E. Corbel, Y. Corre, S. Costea, X. Courtois, T. Czarski, R. Daniel, J. Daumas, M.D. Combarieu, G.D. Temmerman, P.D. Vries, C. Dechelle, F. Deguara, R. Dejarnac, J. Delaplanche, L. Delgado-Aparicio, E. Delmas, L. Delpech, C. Desgranges, P. Devynck, S. Di Genova, R. Diab, A. Diallo, M. Diez, G. Dif-Pradalier, M. Dimitrova, B. Ding, T. Dittmar, L. Doceul, M. Domenes, D. Douai, H. Dougnac, X. Duan, L. Dubus, N. Dumas, R. Dumont, F. Durand, A. Durif, A. Durocher, F. Durodié, A. Ekedahl, D. Elbeze, S. Ertmer, A. Escarguel, F. Escourbiac, K. Ezato, F. Faisse, N. Faure, N. Fedorczak, P. Fejoz, C. Fenzi-Bonizec, F. Ferlay, M. Firdaouss, L. Fleury, D. Flouquet, A. Gallo, Y. Gao, X. Garbet, J. Garcia, J. Gardarein, L. Gargiulo, P. Garibaldi, S. Garitta, J. Gaspar, E. Gauthier, P. Gavila, S. Gazzotti, F. Gely, M. Geynet, S. Gharafi, P. Ghendrih, I. Giacalone, C. Gil, S. Ginoux, S. Girard, E. Giroux, G. Giruzzi, C. Goletto, M. Goniche, T. Gray, E. Grelier, H. Greuner, E. Grigore, C. Grisolia, A. Grosjean, A. Grosman, D. Guibert, D. Guilhem, C. Guillemaut, B. Guillermin, R. Guirlet, J. Gunn, Y. Gunsu, T. Gyergyek, A. Hakola, J. Harris, J. Hatchressian, W. Helou, P. Hennequin, C. Hernandez, K. Hill, J. Hillairet, T. Hirai, G. Hoang, M. Houry, T. Hutter, F. Imbeaux, N. Imbert, I. Ivanova-Stanik, R. Jalageas, A. Jardin, L. Jaubert, G. Jiolat, A. Jonas, P. Joubert, A. Kirschner, C. Klepper, M. Komm, M. Koubiti, J. Kovacic, M. Kozeiha, K. Krieger, K. Krol, B. Lacroix, L. Laguardia, V. Lamaison, H. Laqua, C. Lau, Y. Lausenaz, R. Lé, M.L. Bohec, N. Lefevre, N. Lemoine, E. Lerche, M. Lewerentz, Y. Li, M. Li, A. Liang, P. Linczuk, C. Linsmeier, M. Lipa, X. Litaudon, X. Liu, J.

Llorens, T. Loarer, A. Loarte, T. Loewenhoff, G. Lombard, J. Lore, P. Lorenzetto, P. Lotte, M. Lozano, B. Lu, R. Lunsford, G. Luo, P. Magaud, P. Maget, J. Mahieu, P. Maini, P. Malard, K. Malinowski, P. Manas, L. Manenc, Y. Marandet, J. Marechal, S. Marek, C. Martin, E. Martin, A. Martinez, P. Martino, D. Mazon, P. Messina, L. Meunier, D. Midou, Y. Mineo, M. Missilian, R. Mitteau, B. Mitu, P. Mollard, V. Moncada, T. Mondiere, J. Morales, M. Moreau, P. Moreau, Y. Moudden, G. Moureau, D. Mouyon, M. Muraglia, A. Nagy, T. Nakano, E. Nardon, A. Neff, F. Nespoli, J. Nichols, S. Nicollet, R. Nouailletas, M. Ono, V. Ostuni, C. Parish, H. Park, H. Parrat, J. Pascal, B. Pégourié, F. Pellissier, Y. Peneliau, M. Peret, Y. Peysson, E. Pignoly, G. Pintsuk, R. Pitts, C. Pocheau, C. Portafaix, M. Poulos, P. Prochet, A.P. Sitjes, M. Rasinski, G. Raup, X. Regal-Mezin, C. Reux, B. Riccardi, J. Rice, M. Richou, F. Rigollet, H. Roche, J. Romazanov, C. Ruset, R. Sabot, A. Saille, R. Sakamoto, T. Salmon, F. Samaille, A. Santagiustina, B. Santraine, Y. Sarazin, E. Serre, H. Shin, S. Shiraiwai, J. Signoret, J. Signoret, A. Simonin, O.S. Fettachi, Y. Song, A. Spring, P. Spuig, S. Sridhar, B. Stratton, C. Talatizi, P. Tamain, R. Tatali, M. Téna, A. Torre, L. Toulouse, J. Travère, W. Treutterer, E. Tsitrone, E. Unterberg, G. Urbanczyk, D.V. Eester, G.V. Rooij, S. Vartanian, J. Verger, L. Vermare, D. Vézinet, N. Vignal, B. Vincent, S. Vives, D. Volpe, G. Wallace, E. Wang, L. Wang, Y. Wang, Y. Wang, T. Wauters, B. Wirth, M. Wirtz, A. Wojenski, J. Wright, M. Xu, Q. Yang, H. Yang, B. Zago, Zagorski, B. Zhang, X. Zhang, X. Zou, Operating a full tungsten actively cooled tokamak: overview of WEST first phase of operation, Nucl. Fusion 62 (4) (2022) 042007, http://dx.doi.org/10.1088/1741-4326/ac2525.

[3] K. Tani, M. Azumi, H. Kishimoto, S. Tamura, Effect of toroidal field ripple on fast ion behavior in a tokamak, J. Phys. Soc. Japan 50 (5) (1981) 1726–1737.

[4] V. Thompson, W. Worraker, Divertor target engineering for fusion reactors, Fusion Eng. Des. 13 (2) (1990) 187–199.

[5] J. Bernardo, C. Fenzi, C. Bourdelle, Y. Camenen, H. Arnichand, J.P. Bizarro, S. Cortes, X. Garbet, Z. Guimaraes-Filho, T. Aniel, et al., Density impact on toroidal rotation in Tore Supra: experimental observations and theoretical investigation, Plasma Phys. Control. Fusion 57 (3) (2015) 035002.

[6] D. Moiraf, J. Morales, L. Colas, N. Fedorczak, J. Gaspar, R. Dumont, W. Team, et al., Optimization of the operational domain for ICRH scenarios in WEST from statistical analysis, Nucl. Fusion 63 (8) (2023) 086010.

[7] S. Di Genova, A. Gallo, N. Fedorczak, H. Yang, G. Ciraolo, J. Romazanov, Y. Marandet, H. Bufferand, C. Guillemaut, J. Gunn, et al., Modelling of tungsten contamination and screening in WEST plasma discharges, Nucl. Fusion 61 (10) (2021) 106019.

[8] C.C. Klepper, T. Uckan, P.K. Mioduszewski, R.T. McGrath, P. Hertout, Consideration of the magnetic field ripple in the design of plasma edge components for Tore Supra, Fusion Technol. 14 (2P1) (1988) 288–298.

[9] V. Basiuk, L.-G. Eriksson, V. Bergeaud, M. Chantant, G. Martin, F. Nguyen, R. Reichle, J. Vallet, L. Delpeche, F. Surle, Ripple losses during ICRF heating in Tore Supra, Nucl. Fusion 44 (1) (2003) 181.

[10] K. Tobita, T. Nakayama, S. Konovalov, M. Sato, Reduction of energetic particle loss by ferritic steel inserts in ITER, Plasma Phys. Control. Fusion 45 (2) (2003) 133.

[11] G. Ramogida, G. Calabrò, V. Cocilovo, F. Crescenzi, F. Crisanti, A. Cucchiaro, G. Di Gironimo, R. Fresa, V. Fusco, P. Martin, et al., Active toroidal field ripple compensation and MHD feedback control coils in FAST, Fusion Eng. Des. 88 (6–8) (2013) 1156–1160.

[12] H. Bufferand, C. Baudoin, J. Bucalossi, G. Ciraolo, J. Denis, N. Fedorczak, D. Galassi, P. Ghendrih, R. Leybros, Y. Marandet, N. Mellet, J. Morales, N. Nace, E. Serre, P. Tamain, M. Valentinuzzi, Implementation of drift velocities and currents in SOLEDGE2D–EIRENE, Nucl. Mater. Energy 12 (2017) 852–857, http://dx.doi.org/10.1016/j.nme.2016.11.031, URL https://www.sciencedirect.com/science/article/pii/S2352179116301946, Proceedings of the 22nd International Conference on Plasma Surface Interactions 2016, 22nd PSI.

[13] H. Bufferand, J. Balbin, S. Baschetti, J. Bucalossi, G. Ciraolo, P. Ghendrih, R. Mao, N. Rivals, P. Tamain, H. Yang, et al., Implementation of multi-component Zhdanov closure in SOLEDGE3X, Plasma Phys. Control. Fusion 64 (5) (2022) 055001.

[14] V. Quadri, P. Tamain, Y. Marandet, H. Bufferand, N. Rivals, G. Ciraolo, G. Falchetto, R. Düll, H. Yang, Self-organization of plasma edge turbulence in interaction with recycling neutrals, Contrib. Plasma Phys. (2024) e202300146.

[15] N. Rivals, P. Tamain, Y. Marandet, X. Bonnin, H. Bufferand, R.A. Pitts, G. Falchetto, H. Yang, G. Ciraolo, SOLEDGE3X full vessel plasma simulations for computation of ITER first-wall fluxes, Contrib. Plasma Phys. 62 (5–6) (2022) e202100182.

[16] L. De Gianni, G. Ciraolo, G. Giruzzi, G. Falchetto, N. Rivals, L. Balbinot, N. Varadarajan, S. Sureshkumar, J.-F. Artaud, H. Bufferand, et al., Core and edge modeling of JT-60SA H-mode highly radiative scenarios using SOLEDGE3X-EIRENE and METIS codes, Front. Phys. 12 (2024) 1422286.

[17] G. Ciraolo, S. Di Genova, H. Yang, A. Gallo, N. Fedorczak, H. Bufferand, J. Gunn, P. Tamain, R. Guirlet, C. Guillemaut, et al., Interpretative modeling of impurity transport and tungsten sources in WEST boundary plasma, Nucl. Fusion 61 (12) (2021) 126015.

[18] N. Rivals, P. Tamain, Y. Marandet, X. Bonnin, H. Bufferand, R.A. Pitts, G. Falchetto, H. Yang, G. Ciraolo, Impact of enhanced far-SOL transport on first wall fluxes in ITER from full vessel edge-plasma simulations, Nucl. Mater. Energy 33 (2022) 101293.

[19] H. Yang, Control of Detachment in the Divertor Region of Tokamaks: Impact of Wall Geometry, Particle, and Energy Sources (Ph.D. thesis), Aix-Marseille University, 2023.

[20] S. Di Genova, Heavy Ions Migration in Tokamak Boundary Plasmas : Development of a Numerical Model to Interpret WEST Experiments (Ph.D. thesis), Aix-Marseille University, 2023.

[21] R. Düll, H. Bufferand, E. Serre, G. Ciraolo, V. Quadri, N. Rivals, P. Tamain, Introducing electromagnetic effects in Soledge3X, Contrib. Plasma Phys. (2024) e202300147.

[22] S.I. Braginskii, Transport processes in a plasma, Rev. Plasma Phys. 1 (1965) 205.

[23] P. Ghendrih, T. Cartier-Michaud, G. Dif-Pradalier, D. Esteve, X. Garbet, V. Grandgirard, G. Latu, C. Norscini, Y. Sarazin, Collisions in magnetised plasmas, ESAIM: Proc. Surv. 50 (2015) 81–112.

[24] L. Spitzer Jr., R. Härm, Transport phenomena in a completely ionized gas, Phys. Rev. 89 (5) (1953) 977.

[25] V.M. Zhdanov, Transport Processes in Multicomponent Plasma, CRC Press, 2002.

[26] M. Raghunathan, Y. Marandet, H. Bufferand, G. Ciraolo, P. Ghendrih, P. Tamain, E. Serre, Multi-temperature generalized zhdanov closure for scrape-off layer/edge applications, Plasma Phys. Control. Fusion 64 (4) (2022) 045005.

[27] H. Bufferand, J. Bucalossi, G. Ciraolo, G. Falchetto, P. Gallo, N. Rivals, P. Tamain, H. Yang, G. Giorgiani, F. Schwander, M. Scotto D'Abusco, E. Serre, Y. Marandet, M. Raghunathan, W. Team, J. Team, Progress in edge plasma turbulence modelling—hierarchy of models from 2D transport application to 3D fluid simulations in realistic tokamak geometry, Nucl. Fusion 61 (11) (2021) 116052.

[28] R. Düll, A 3D Electromagnetic Model in SOLEDGE, 2024.

[29] F. Iannone, G. Bracco, C. Cavazzoni, R. Coelho, D. Coster, O. Hoenen, A. Maslennikov, S. Migliori, M. Owsiak, A. Quintiliani, B. Palak, V. Pais, F. Robin, E. Rossi, I. Voitsekhovitch, MARCONI-FUSION: The new high-performance computing facility for European nuclear fusion modelling, Fusion Eng. Des. 129 (2018) 354–358, http://dx.doi.org/10.1016/j.fusengdes.2017.11.004, URL https://www.sciencedirect.com/science/article/pii/S0920379617309018.